

ENGINEERING

Uncooled self-powered hemispherical biomimetic pit organ for mid- to long-infrared imaging

Yucheng Ding^{1,2,3,4,†}, Gongze Liu^{5,†}, Zhenghao Long^{1,3,4}, Yu Zhou^{1,3,4}, Xiao Qiu^{1,3,4}, Beitao Ren^{1,3,4}, Qianpeng Zhang^{1,3,4}, Cheng Chi⁵, Zhu'an Wan^{1,3,4}, Baoling Huang^{5*}, Zhiyong Fan^{1,3,4,6*}

Infrared vision is highly desirable for applications in multifarious fields. Of the few species with this visual capability, snakes have exceptional infrared perception with the assistance of pit organs. Inspired by the pit organ design we present here a hemispherical biomimetic infrared imaging device. The devices use high-density ionic thermoelectric polymer nanowire arrays that serve as the sensing nerve cells. The individual nanowires exhibit notable voltage response to temperature variation in test objects. An infrared sensor array with 625 pixels on the hemispherical substrate is successfully demonstrated with an ultrawide field of view up to 135°. The device can image body temperature objects without a cooling system and external power supply. This work opens up opportunities for the design and fabrication of bioinspired infrared imaging devices based on emerging ionic thermoelectric materials.

INTRODUCTION

Infrared (IR) vision is a rare visual capability bestowed upon very few species on Earth. For instance, pit vipers rely on their IR imaging device, i.e., pit organs, to hunt for warm-blooded small animals (1–3). Amazingly, a pit organ only uses a simple optical system comprising a pinhole lens and a curved pit membrane IR imager whose function is akin to the hemispherical retina in a human eye for visible light sensing. The pit membrane has ~7000 of IR-sensing cells that provides sufficient resolution (4), and a pit organ has a wide field of view (FoV) of around 100° (5). On the other hand, IR image sensors have very broad applications in reality, covering medical instrumentation, surveillance, environmental monitoring, robotics, and space exploration. Notable progress has been made in recent years owing to the development of new IR materials. Among them, the emerging ionic thermoelectric (*i*-TE) materials (6–11) exhibit an ultrahigh Seebeck coefficient and low thermal conductivity as compared with the conventional IR sensing materials such as polysilicon. Meanwhile, the vast majority of the existing IR imaging devices are still based on planar sensor arrays, unlike their biological counterparts (12–16). The planar IR image sensors not only have small limited FoV, typically <90°, but also require multiple lenses to flatten the image plane due to the Petzval field curvature. This leads to sophisticated and costly device design and compromised IR sensing performance due to transmittance loss. Inspired by pit organ design, integrating IR sensors on a curved surface can be a potential solution to address this issue. Curved IR image sensors can effectively

eliminate imaging aberrations by fitting the focal plane well. Meanwhile, the simplified optical design minimizes the IR transmittance loss, thus preserving the detection sensitivity in addition to reducing the form factor of the IR devices. However, curved substrates are incompatible with the conventional device fabrication processes, which entail an enormous challenge on device fabrication and sensor integration (17). Thus, there is nearly no report on highly curved IR image sensors that can detect mid- to long-IR bands, to our best knowledge.

Here, we demonstrate a biomimetic hemispherical polymer-based ionic thermoelectric (PIT) image sensor with 625 pixels. It consists of high-density *i*-TE polymer nanowire array. These nanowires exhibit ultrahigh thermopower with subtle temperature difference and can effectively mimic thermal receptors in pit organs. Aided by an IR-absorbing layer, our PIT image sensor can detect and image mid- to long-wavelength IR light at room temperature. The thermoelectric effect enables self-powered working mode of the device, exhibiting a high responsivity (0.5 mV for a 40°C object at 5-cm distance) and a reasonable response rate of 0.69 s. The hemispherical nature of the device renders an ultrawide FoV of 135°, which is much larger than that of the pit organ. We further demonstrate that the device can be well used for staring imaging of human hand gestures and heated symbols with ~60°C temperature. Overall, our device mimics the pit organ both structurally and functionally, with the density of nanowire array far exceeding that of the thermal receptors on the pit membrane. It can inspire the design and fabrication of a new type of high-performance IR imaging devices.

RESULTS

Figure 1 shows the comparison between the pit organ (Fig. 1, A to C) and our PIT image sensor (Fig. 1, D to F). Pit organs are located on cheeks of a viper's face, between the eye and the nostril (Fig. 1A). The pit organ has a simple optical structure; essentially, it is a pinhole camera, consisting of an IR image sensor (pit membrane) and a lensless aperture. In the cross-sectional view, the curved pit membrane, which serves as an IR antenna, has two cavities on each side and massive blood vessels and nerves on the membrane. The thermal receptors formed by terminal nerve masses are innervated by primary afferent nerve fibers and generate neuroelectric signals that

¹Department of Electronic and Computer Engineering, The Hong Kong University of Science and Technology, Clear Water Bay, Kowloon, Hong Kong SAR, China. ²Microelectronics Thrust, The Hong Kong University of Science and Technology (Guangzhou), Nansha, Guangzhou, Guangdong, China. ³State Key Laboratory of Advanced Displays and Optoelectronics Technologies, HKUST, Clear Water Bay, Kowloon, Hong Kong SAR, China. ⁴Guangdong-Hong Kong-Macao Joint Laboratory for Intelligent Micro-Nano Optoelectronic Technology, HKUST, Clear Water Bay, Kowloon, Hong Kong SAR, China. ⁵Department of Mechanical and Aerospace Engineering, The Hong Kong University of Science and Technology, Clear Water Bay, Kowloon, Hong Kong SAR, China. ⁶Department of Chemical and Biological Engineering, The Hong Kong University of Science and Technology, Clear Water Bay, Kowloon, Hong Kong SAR, China.

*Corresponding author. Email: eezfan@ust.hk (Z.F.); mebh Huang@ust.hk (B.H.)

†These authors contributed equally to this work.

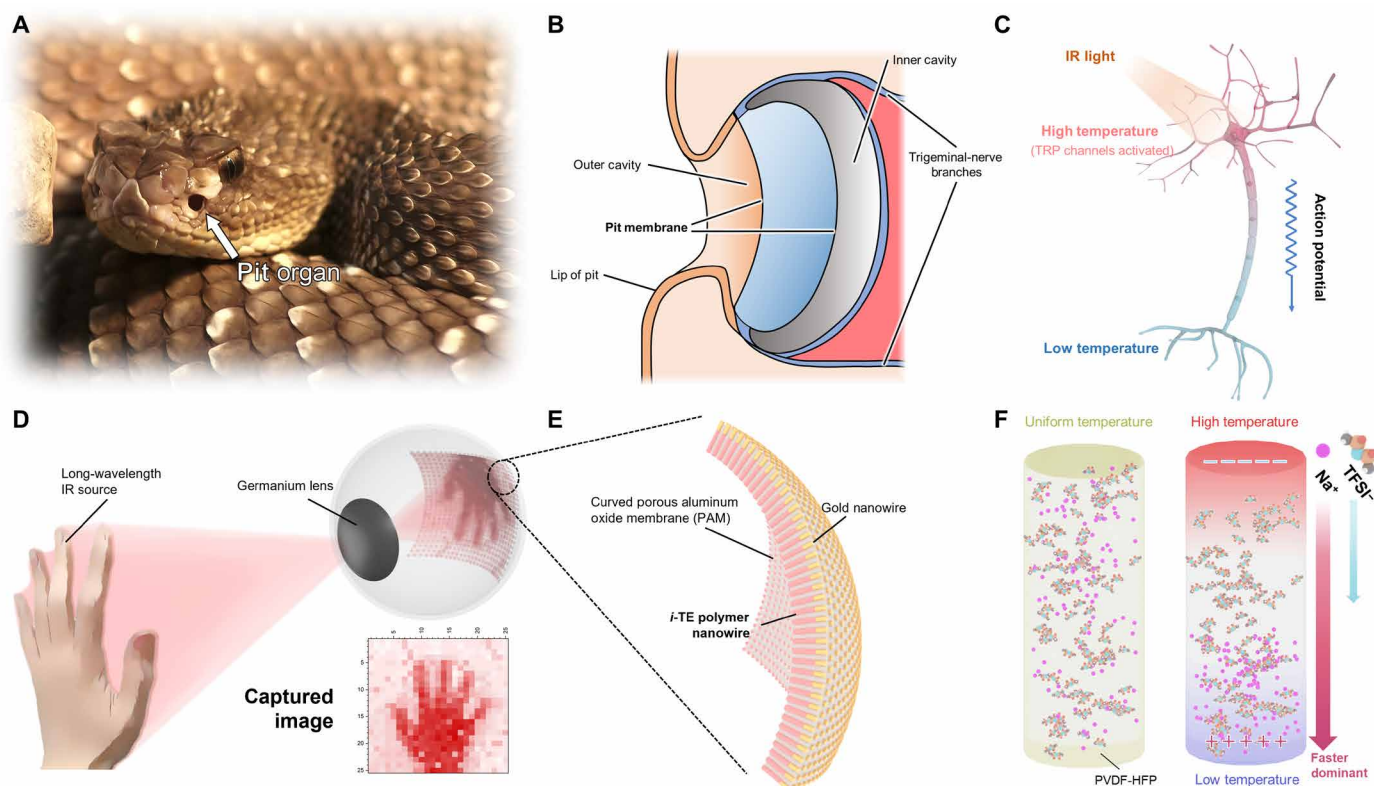


Fig. 1. Overall comparison of pit organ and our PIT image sensor. (A) Photograph of a pit viper showing the location of pit organ with white arrow. (B) Schematic of the pit organ from a cross-sectional view. (C) Schematic of the terminal nerve masses. They generate action potentials according to the temperature difference caused by IR light. TRP, transient receptor potential. (D to F) Schematic of the working mechanism of PIT device (D), *i*-TE polymer nanowires in the curved PAM (E), and p-type *i*-TE material (F). PVDF-HFP, polyvinylidene fluoride–hexafluoropropylene. Copyright: (A) by James Arup Photography is licensed under CC BY 2.0.

are transmitted via the trigeminal nerve to the optic tectum of the viper's brain. In this region of the brain, signals from the pit organ can be complemented by other visual signals. Although the pit organ has many similarities to the retina, it does not directly detect IR light. A pit organ contains a temperature-sensitive transient receptor potential (TRP) channel, TRPA1 (18). In the presence of IR light, the surface temperature of the pit membrane increases slightly, which triggers responses of TRPA1. The temperature-sensitive receptors on the pit organ can detect a temperature difference as small as 0.001°C with respect to the organ itself (19), according to previous reports. Our PIT image sensor mimics the pit organ, and its structure was further optimized to fit practical applications (Fig. 1D). Specifically, a single germanium lens is installed to filter visible light and focus IR light. Simultaneously, the spherical enclosed structure avoids interference from air convection. These optimizations ensure high-quality imaging. The core component of our device, the IR image sensor, is an *i*-TE polymer nanowire array rooted in a self-assembled porous alumina membrane (PAM) (Fig. 1E). The thermoelectric effect enables direct conversion of temperature gradient to an electric voltage under the thermodiffusion of mobile charge carriers. Different from the conventional semiconductor thermoelectric materials, *i*-TE polymer uses ionic charge carriers to convert temperature gradient into a static electric voltage under the Soret effect. To be distinguished from the conventional Seebeck effect that is electron/hole dominated, the effect herein is defined as the ionic Seebeck effect (20). For p-type materials, the thermal mobility of cation (Na⁺)

is higher than that of anion (TFSI⁻); thus, the thermodiffusion of cations will dominate, as shown in Fig. 1F, while n-type materials, in which cations are captured by additives, are dominated by the thermodiffusion of anions. Although *i*-TE materials cannot be used for temperature differential power generation because of their low electrical conductivity, it is particularly suitable for IR sensing as only photovoltage is required here. Furthermore, *i*-TE materials are virtually nontoxic and environmentally friendly, with advantages in terms of Seebeck coefficients over other conventional solid-state semiconductor thermoelectric materials (table S1), which usually contain heavy metals.

Figure 2 shows the configuration of the PIT image sensor. From frontside to backside are the germanium lens, the front hemispherical shell (Fig. 2C), the SiO₂ IR-absorbing layer, the frontside Cu common electrode (Fig. 2D), the nanowire array (Fig. 2, E and F), the socket to assemble metal microwires, and the back-contact microwire electrodes. The absorption and transmission spectra of the germanium and IR absorber layer are shown in figs. S1 and S2. Germanium has high light transmittance in the wavelength range of 7 to 14 μm and is opaque to visible light. In contrast, the IR-absorbing layer effectively absorbs light in the long-wavelength IR band. The back-contact electrodes, namely, nickel microwires, are assembled by magnetic field-assisted alignment (Fig. 2G and fig. S4). The socket helps to position the electrodes and facilitate manual assembly of the microwires. Note that nickel microwires are dipped in melted gallium before placement to improve the contact, as shown in Fig. 2H. These nickel microwires

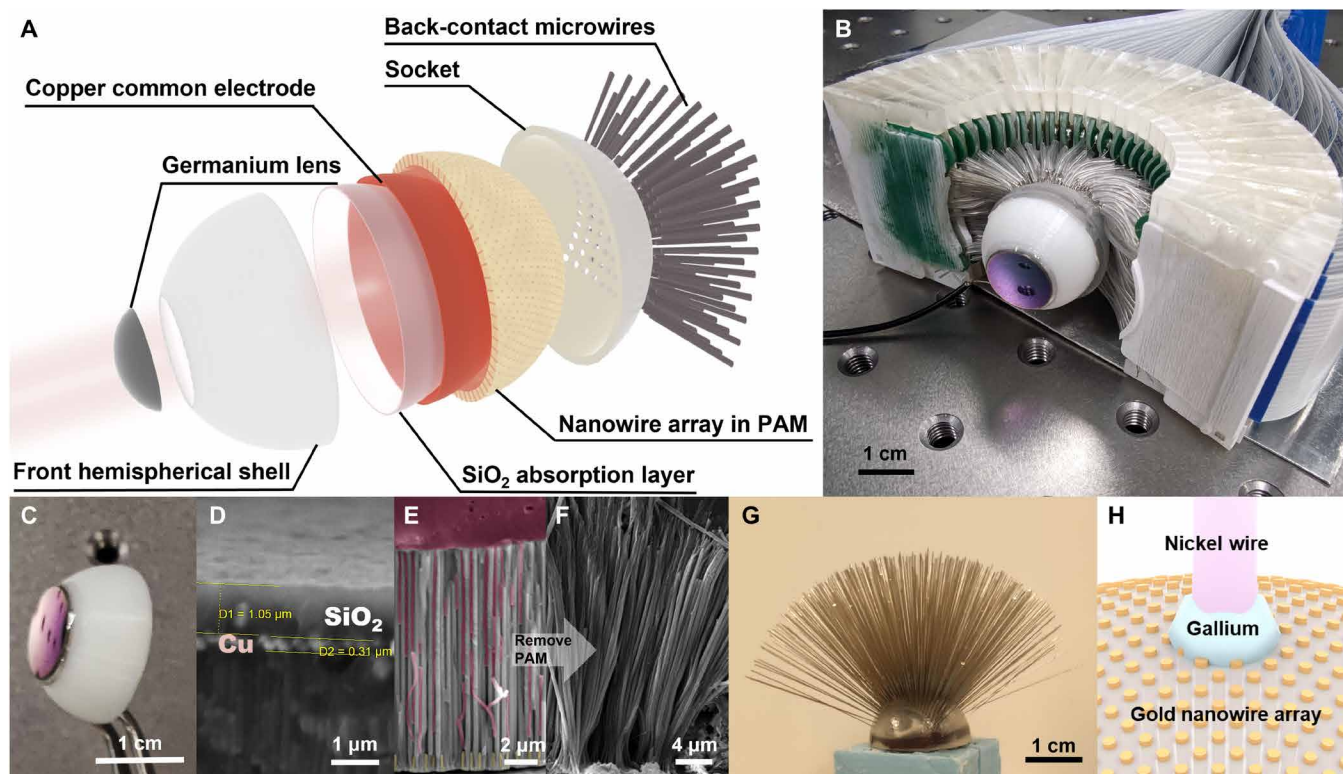


Fig. 2. Detailed structure of the PIT Device. (A) Exploded schematic of PIT device. Photograph of the PIT image sensor (B) and the germanium lens (C). Cross-sectional scanning electron microscopy (SEM) image of front layers (D) and *i*-TE polymer nanowires in PAM (E). (F) Freestanding *i*-TE polymer nanowires. (G) Photograph of the magnetic field–assisted alignment. (H) Schematic of the back contact between nickel wires and gold nanowire array.

are further encapsulated with rubber hoses to avoid short circuits and then soldered to the printed circuit board (PCB) to enable signal acquisition. This connection is similar to that of the pit organ, whereby the thermal sensor is connected to the nerve fibers, effectively avoiding cross-talk and allowing signals to be transmitted in parallel. As the reading circuit is located behind the sensing material, its interference on the imaging is avoided. Using this approach, we have successfully prepared a 625-pixel hemispherical IR image sensor with a minimum pitch of 550 μm . Because of the accuracy limit of manual assembly, it is difficult to further increase pixel density. Nonetheless, with the aid of high-precision programmable robotic arms in the future, the pitch can be readily reduced, and thus, the pixel numbers can be increased.

Our PIT device is distinctly different when compared with the existing uncooled IR focal plane arrays (FPAs) on mechanism and fabrication process. Current uncooled IR FPAs are usually based on microbolometer (21). The resistance value of commonly used materials, such as VO_x or $\alpha\text{-Si}$, varies with temperature. They are passive devices and require external power supplies to read the signal. In contrast, the PIT image sensor is based on the *i*-TE effect and can generate an electrical potential difference according to temperature difference. It is naturally a self-powered device with no energy consumption. In addition, because the magnitude of the voltage signal is only related to the ion distribution in the vertical direction, its signal strength does not decrease much when reducing the pixel size, which is different from devices that rely on electrical current signals. Theoretically, each nanowire in our PIT device can work as an individual pixel without any concern about the signal strength. As

far as fabrication process is concerned, VO_x or $\alpha\text{-Si}$ films highly rely on various deposition methods and equipment. In stark contrast, *i*-TE polymers are compatible with solution methods, and the preparation process is facile and flexible. Specifically, *i*-TE polymers can be filled into the PAM pores by spin coating, and discrete nanowires can be readily obtained after O_2 plasma etching.

PAMs are unique nanoporous templates for integrated nano-electronics and nano-optoelectronics, owing to their stable physico-chemical properties and excellent electrical insulation properties (22–24). Their form factors, such as shape, thickness, pore size, and pore pitch, can be well engineered, which facilitates highly versatile device design. Here, hemispherical PAMs are fabricated to integrate *i*-TE polymer nanowires. The aluminum oxide nanochannels not only guide the formation of nanowires but also prevent the lateral transport of ions, thus improving the responsivity. In addition, the length of the nanowires is determined by the thickness of the PAM and can vary from 1 to 80 μm with excellent uniformity, which is not achievable for *i*-TE polymer thin films deposited on planar substrates (figs. S5 and S6). The pitch of the nanowires is about 500 nm (Fig. 2E), which is less than the diffraction limit in the IR band, indicating that PAM-based nanowire arrays have the potential to achieve ultrahigh-resolution imaging. The imaginable downside of PAM is that because of the relatively high thermal conductivity of alumina (25), as compared to the polymer itself, the undesirable lateral thermal diffusion may undermine the temperature difference between the two ends of the nanowires and thus affect the device performance. However, from the high-resolution scanning electron microscopy (SEM) images, we noticed that the *i*-TE nanowires are not

firmly fitted to the PAM nanochannel sidewall (fig. S8), which can be attributed to volume shrinkage caused by solvent evaporation during annealing. This detaching phenomenon may reduce lateral thermal conduction and thus favors device performance. In addition, in thin films, this phenomenon often manifests itself in the form of widely present pinholes.

Figure 3A presents the voltage difference of the p-type *i*-TE material under alternating temperature gradients (ΔT). It is measured with a homemade in-plane setup (fig. S9) and proves that the thermoelectric response is fast and repeatable. Figure 3B shows the thermopower of p/n-type *i*-TE materials versus temperature gradient, which is derived from the responses in Fig. 3A and fig. S10. The response of both materials exhibits a fine linearity with temperature gradient when ΔT is below 5 K. The following test results indicate that the internal temperature gradient of the device under regular operating scenarios is within 5 K and does not exceed the linear range of *i*-TE material.

We further built a setup (fig. S11) to measure the performance of individual pixels. Visible to near-IR light was first used as a source because it could be directly observed for better tracking and focusing. Figure 3C illustrates the transient response of an individual pixel under chopped visible to near-IR light with peak wavelength at 830 nm. The highly repeatable response indicates the excellent stability and reproducibility of the device. Figure 3D shows that the device has a response time of 0.69 s and a recovery time of 0.83 s by intercepting a light-dark cycle. Limited by the relatively low speed of heat conduction, the response time of thermal IR detectors is not comparable to that of the photonic IR detectors, which is due to the

difference on operating principle. The limitation of the ion migration rate prolongs the response time. However, reducing nanowire length can expedite the response because of shortened ion diffusion path. Figure 3E shows the response of an individual pixel to a temperature-tunable blackbody furnace at 5-cm distance. Thermal voltage is positively correlated with the temperature of the blackbody (Fig. 3F). Moreover, a thermo-induced voltage of 500 μ V can be achieved for a blackbody at 40°C. The excellent performance of the device allows the signal to be acquired efficiently. Because nanowires are connected in parallel with each other, the response of an individual pixel with sufficiently small size is approximately equal to that of a single nanowire, providing the potential for further improvement in pixel density.

On the basis of the respectable performance of individual pixels, we evaluated the IR imaging capabilities of the entire PIT device. Figure 4A shows an overall schematic of the testing setup, in which the 625 pixels of PIT device are connected to a computer-controlled multiplexer via PCBs. More details about the connection are shown in fig. S12. Figure 4B and fig. S13 illustrate the response of the device to the blackbody furnace with different temperatures. The response of the different pixels is in good consistency at the same temperature, and the voltage signal of the device is positively correlated with temperature. The hemispherical PIT device ensures a wider FoV than conventional planar IR image sensors. The diagonal visual field of PIT device is about 135°, whereas that of a planar device is only 87°, as is shown in Fig. 4C. We further used the PIT device to image human hand gestures at room temperature (Fig. 4, D to F). The output images exhibit good contrast and can

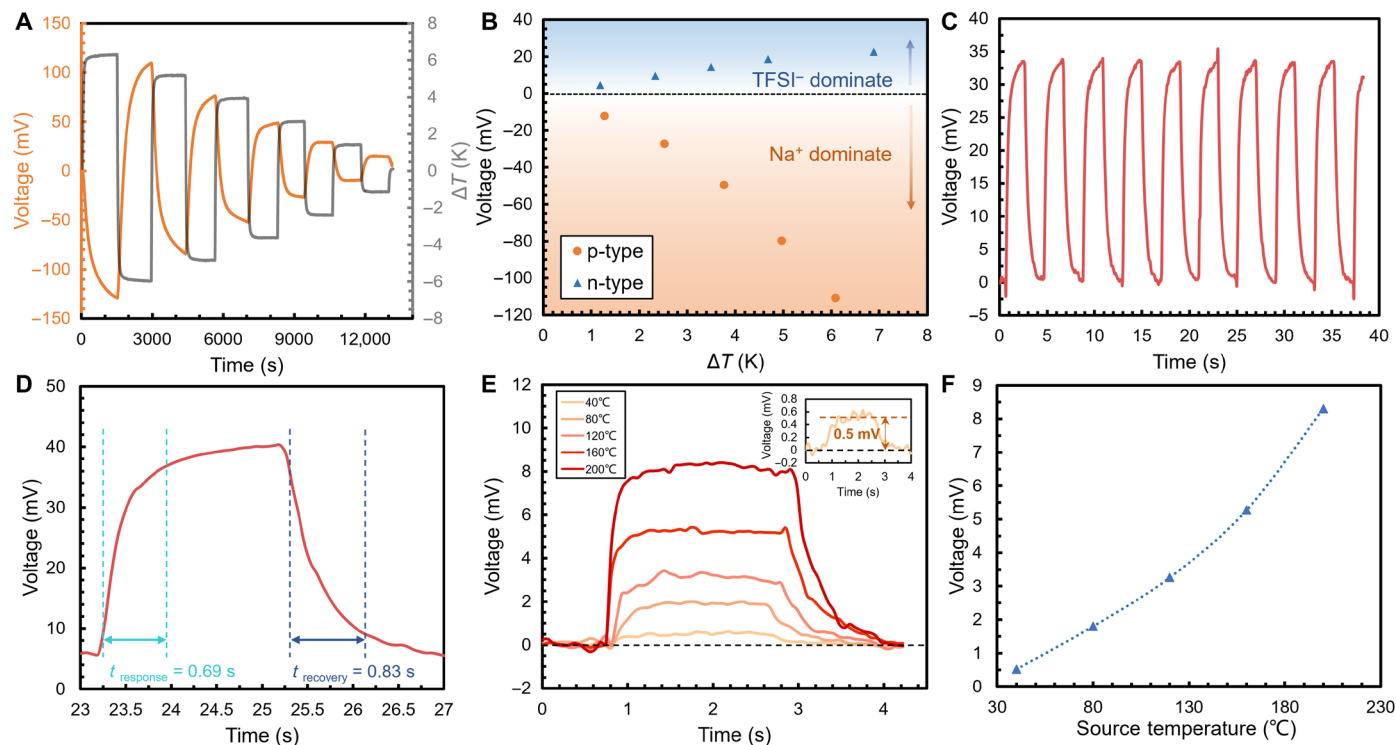


Fig. 3. Characterization of thermopower of *i*-TE material and performance of individual pixel. (A) Voltage difference of p-type *i*-TE material under alternating temperature gradients. (B) Voltage-temperature difference plot of p- and n-type *i*-TE material. (C) Response of individual pixel to chopped light. (D) Response speed analysis of individual pixel with chopped light. (E) Response of individual pixel to blackbody furnace at 5-cm distance from 40° to 200°C. The inset plots the response to 40°C blackbody furnace individually. (F) Voltage-temperature curve of individual pixel.

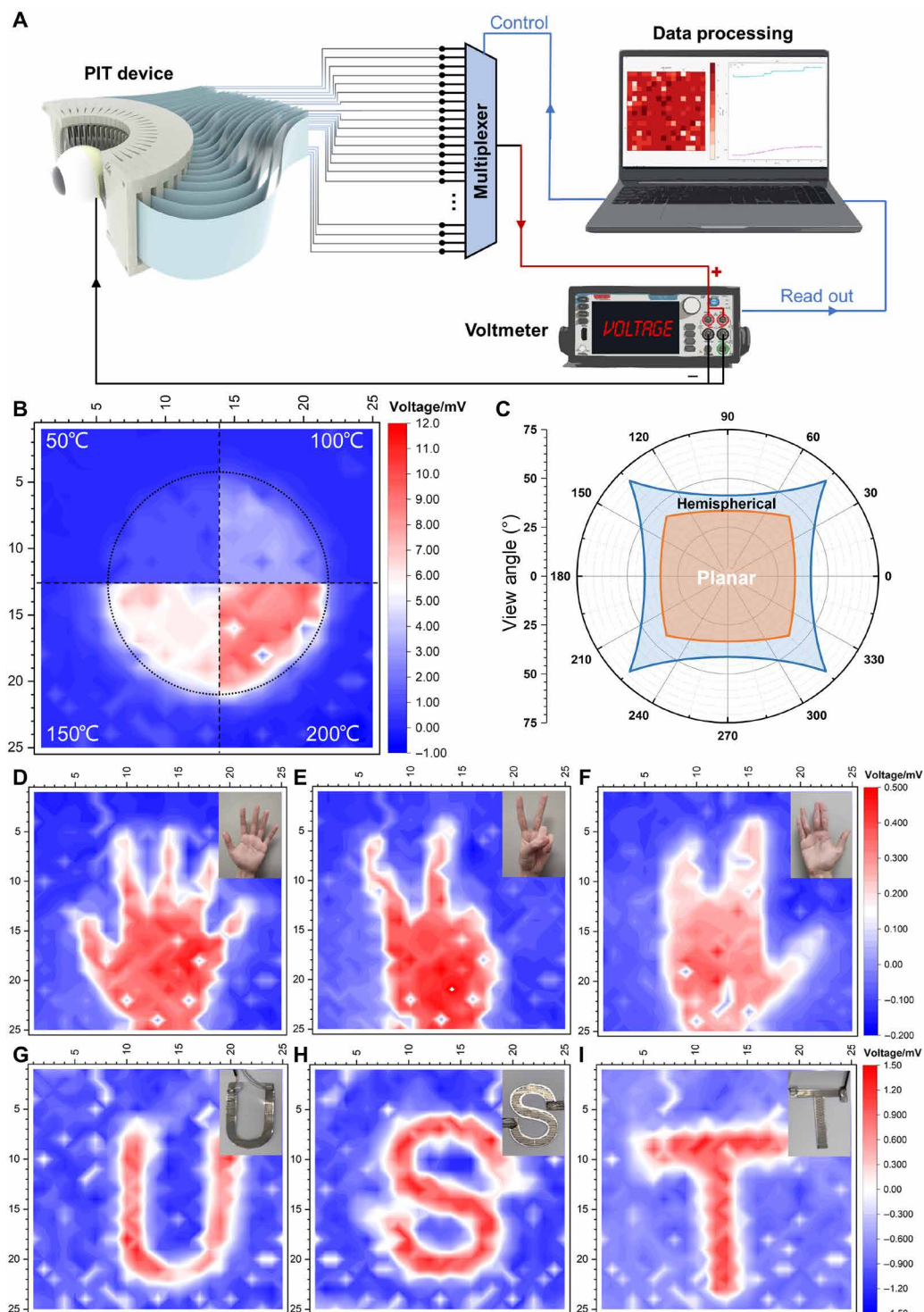


Fig. 4. IR-imaging demonstration with 625-pixel PIT device. (A) Schematic of measurement setup. (B) A combination of images of blackbody furnace at different temperature captured by PIT device. (C) Calculated FoV comparison of hemispherical device and planar device with an image distance of 1 cm. (D to F) Captured images of human hand at room temperature. (G to I) Captured images of letter-shaped resistors with a semiconductor chilling plate ($\sim 0^{\circ}\text{C}$) as the background. Insets provide the optical photos of imaging target.

clearly identify different hand gestures without the assistance of algorithms. This proves that the PIT device is capable of detecting and imaging body temperature objects at room temperature. In addition, we prepared a few letter-shaped resistors by inkjet printing (fig. S14), which were then used as heated objects for IR imaging. Figure 4 (G to I) shows the captured images of letters “U,” “S,” and “T.” Movie S1 shows the instant images acquired by PIT device, capturing the heating up and cooling down processes corresponding to letter T.

DISCUSSION

Here, we demonstrate an uncooled self-powered biomimetic IR image sensor based on emerging ionic polymer composite nanowires. The device has an ultrawide FoV with capability to image human body temperature objects. The work here can open up a new pathway to design and fabricate bioinspired novel IR imaging devices with emerging materials.

MATERIALS AND METHODS

Materials

Polyvinylidene fluoride–hexafluoropropylene (PVDF-HFP) pellets (average molecular weight, $455,000 \text{ g mol}^{-1}$), sodium bis(trifluoromethylsulfonyl)imide (NaTFSI), propylene carbonate (PC, anhydrous, 99.7%), *N*-methyl-2-pyrrolidone (NMP; high-performance liquid chromatography, $\geq 99\%$), and tris(pentafluorophenyl)borane (TPFPB, min. 97%) were purchased from Sigma-Aldrich. All the materials were stored in the glovebox without any additional treatment.

Preparation of *i*-TE material precursor solution

PVDF-HFP pellets were firstly dried in an oven at 100°C for 24 hours and were dissolved in NMP at a concentration of 0.1 g ml^{-1} . The p-type precursor solution was prepared by mixing 1 M NaTFSI per PC solution with mass ratios of 86 weight % and NMP solution with PVDF-HFP pellets in an argon atmosphere. The mixture was stirred with rapid magnetic stirring for 8 hours. For n-type material, the precursor solution was prepared by adding 0.25 M TPFPB into p-type precursor solution in an argon atmosphere and stirred for 8 hours at 60°C .

Fabrication of PIT image sensor

Figure S3 shows the schematic of the fabrication process below.

Preparing of hemispherical PAM with gold nanowire array

The fabrication process started with a 2-cm diameter hemispherical aluminum shell, which is deformed from a 0.5-mm-thick aluminum chip. After electropolishing for 10 min, it underwent a two-step anodization process to form a 50- μm -thick PAM with a pitch of 500 nm. The pore size of PAM was enlarged from 160 to 300 nm by wet etching with 5% H_3PO_4 aqueous solution at 54°C for 10 min. Then, a barrier-thinning process and electrochemical deposition of gold were carried out to form a 500-nm nanowire array of gold at the bottom of PAM. The aluminum substrate was wet-etched with FeCl_3 solution to obtain a freestanding hemispherical PAM. NaOH (2%) aqueous solution was applied to the back side of PAM to remove the barrier layer and expose gold nanowires.

Filling p-type *i*-TE material into PAM

The p-type precursor solution was dropped onto the PAM surface. The PAM with solution was evacuated to lower than 1 mbar in a

chamber for 5 min. Then, a spin-coating process was done to remove extra solution with a rotation speed of 2000 rpm. It was annealed at 70°C for 15 min and then treated with O_2 plasma for 30 min to etch the overflowed polymer.

Deposition of common electrode layer and SiO_2 layer

On the front side of PAM, a copper layer of 300-nm thickness was deposited with thermal evaporation at a rate of 5 A/s. Then, a 1- μm -thick SiO_2 layer was deposited with e-beam evaporation at a rate of 10 A/s, in which the edge of PAM was masked to keep the copper layer exposed for further wire bonding.

Magnetic field–assisted assembly of back-contact nickel wires

A 0.2-mm-diameter nickel wire was cut into 3-cm sections as the back-contact electrodes. PAM was combined with a hemispherical socket and then fixed into a homemade setup composed of a stainless-steel ball and a spherical permanent magnet, as shown in fig. S3. Before assembly, nickel wires were dipped in melted gallium to enhance the contact. A total of 625 nickel wires were assembled into the holes on socket and can stand on the surface of PAM with the assistance of magnetic field. Last, ultraviolet epoxy was applied and cured on the socket to fix all the nickel wires firmly.

Assembling of the whole PIT device

Nickel wires were wrapped with rubber hoses and then welded onto PCBs column by column. A series of three-dimensional (3D)–printed brackets were used to fix and combine all the 25 PCBs. On the front side, the copper layer was bonded with conducting wire using silver paste. A germanium lens (diameter, 13 mm; focal length, 15/10 mm) was fixed into a 3D-printed model and then assembled with the device.

Measurement and demonstration

Thermal power test of *i*-TE material thin films

An in-plane setup composed of a heat sink, Peltier elements, glass substrate, and thermocouple was calibrated first and used for ionic thermopower measurement. The starting hot and cool ends of measured samples were electrically connected to the positive and negative poles of a voltmeter, respectively. For p-type material, a negative thermal voltage was generated when a positive temperature difference ($\Delta T = +1$ to 6 K) was applied. The positive thermal voltage is generated when alternating hot and cold ends.

Individual pixel performance measurement

The voltage was measured by Keithley 2450 source meter unit (SMU). A laser diode (peak wavelength, 830 nm; power, 16 to 300 mW; spot diameter, 1 to 5 mm) and a blackbody furnace (BX-350, CEM, China) were used as sources. An optical chopper was used to chop light into square wave.

Demonstration

The PIT device was connected to the SMU through five 128-channel multiplexer units (PXI2530B, National Instruments, USA), which are installed inside a chassis (PXI1031, National Instruments, USA). The whole system was controlled by a home-built Python program.

SUPPLEMENTARY MATERIALS

Supplementary material for this article is available at <https://science.org/doi/10.1126/sciadv.abq8432>

REFERENCES AND NOTES

- H. A. Schraft, G. S. Bakken, R. W. Clark, Infrared-sensing snakes select ambush orientation based on thermal backgrounds. *Sci. Rep.* **9**, 1–6 (2019).
- P. H. Hartline, L. Kass, M. S. Loop, Merging of modalities in the optic tectum: Infrared and visual integration in rattlesnakes. *Science* **199**, 1225–1229 (1978).

3. E. A. Newman, P. H. Hartline, Integration of visual and infrared information in bimodal neurons in the rattlesnake optic tectum. *Science* **213**, 789–791 (1981).
4. E. A. Newman, P. H. Hartline, The infrared “Vision” of snakes. *Sci. Am.* **246**, 116–127 (1982).
5. B. Schwarzschild, Neural-network model may explain the surprisingly good infrared vision of snakes. *Phys. Today* **59**, 18 (2006).
6. C. Chi, M. An, X. Qi, Y. Li, R. Zhang, G. Liu, C. Lin, H. Huang, H. Dang, B. Demir, Y. Wang, W. Ma, B. Huang, X. Zhang, Selectively tuning ionic thermopower in all-solid-state flexible polymer composites for thermal sensing. *Nat. Commun.* **13**, 1–10 (2022).
7. D. Zhao, S. Fabiano, M. Berggren, X. Crispin, Ionic thermoelectric gating organic transistors. *Nat. Commun.* **8**, 1–7 (2017).
8. S. Liu, Y. Yang, H. Huang, J. Zheng, G. Liu, T. H. To, B. Huang, Giant and bidirectionally tunable thermopower in nonaqueous ionogels enabled by selective ion doping. *Sci. Adv.* **8**, 1–9 (2022).
9. D. Zhao, A. Würger, X. Crispin, Ionic thermoelectric materials and devices. *J. Energy Chem.* **61**, 88–103 (2021).
10. C.-G. Han, X. Qian, Q. Li, B. Deng, Y. Zhu, Z. Han, W. Zhang, W. Wang, S. Feng, G. Chen, W. Liu, Giant thermopower of ionic gelatin near room temperature. *Science* **368**, 1091–1098 (2020).
11. D. Zhao, A. Martinelli, A. Willfahrt, T. Fischer, D. Bernin, Z. U. Khan, M. Shahi, J. Brill, M. P. Jonsson, S. Fabiano, X. Crispin, Polymer gels with tunable ionic seebeck coefficient for ultra-sensitive printed thermopiles. *Nat. Commun.* **10**, 1–8 (2019).
12. J. Lee, E. Georgitzikis, Y. Li, Z. Lin, J. Park, I. Lieberman, D. Cheyngs, M. Jayapala, A. Lambrechts, S. Thijs, R. Stahl, P. E. Malinowski, in *2020 IEEE International Electron Devices Meeting (IEDM)*, San Francisco, CA, 12 to 18 December 2020 (IEEE, 2020), pp. 1651–1654; <https://ieeexplore.ieee.org/document/9372018/>.
13. A. Ren, J. Zou, H. Lai, Y. Huang, L. Yuan, H. Xu, K. Shen, H. Wang, S. Wei, Y. Wang, X. Hao, J. Zhang, D. Zhao, J. Wu, Z. Wang, Direct laser-patterned MXene-perovskite image sensor arrays for visible-near infrared photodetection. *Mater. Horizons* **7**, 1901–1911 (2020).
14. R. Kaufmann, G. Isella, A. Sanchez-Amores, S. Neukom, A. Neels, L. Neumann, A. Brenzikofer, A. Dommann, C. Urban, H. Von Känel, Near infrared image sensor with integrated germanium photodiodes. *J. Appl. Phys.* **110**, 023107 (2011).
15. C. Y. Wu, J. W. Kang, B. Wang, H. N. Zhu, Z. J. Li, S. R. Chen, L. Wang, W. H. Yang, C. Xie, L. B. Luo, Defect-induced broadband photodetection of layered γ -In₂Se₃ nanofilm and its application in near infrared image sensors. *J. Mater. Chem. C* **7**, 11532–11539 (2019).
16. M. Shimatani, S. Fukushima, S. Okuda, S. Ogawa, High-performance graphene/InSb heterojunction photodetectors for high-resolution mid-infrared image sensors. *Appl. Phys. Lett.* **117**, 1–6 (2020).
17. D. Dumas, M. Fendler, N. Baier, J. Primot, E. Le Coarer, Curved focal plane detector array for wide field cameras. *Appl. Optics* **51**, 5419–5424 (2012).
18. E. O. Gracheva, N. T. Ingolia, Y. M. Kelly, J. F. Cordero-Morales, G. Holloper, A. T. Chesler, E. E. Sánchez, J. C. Perez, J. S. Weissman, D. Julius, Molecular basis of infrared detection by snakes. *Nature* **464**, 1006–1011 (2010).
19. G. S. Bakken, A. R. Krochmal, The imaging properties and sensitivity of the facial pits of pitvipers as determined by optical and heat-transfer analysis. *J. Exp. Biol.* **210**, 2801–2810 (2007).
20. H. Wang, U. Ail, R. Gabrielsson, M. Berggren, X. Crispin, Ionic Seebeck effect in conducting polymers. *Adv. Energy Mater.* **5**, 1–6 (2015).
21. R. K. Bhan, V. Dhar, Recent infrared detector technologies, applications, trends and development of HgCdTe based cooled infrared focal plane arrays and their characterization. *Opto-Electronics Rev.* **27**, 174–193 (2019).
22. D. Zhang, L. Gu, Q. Zhang, Y. Lin, D. H. Lien, M. Kam, S. Poddar, E. C. Garnett, A. Javey, Z. Fan, Increasing photoluminescence quantum yield by nanophotonic design of quantum-confined halide perovskite nanowire arrays. *Nano Lett.* **19**, 2850–2857 (2019).
23. L. Gu, M. M. Tavakoli, D. Zhang, Q. Zhang, A. Waleed, Y. Xiao, K. H. Tsui, Y. Lin, L. Liao, J. Wang, Z. Fan, 3D Arrays of 1024-pixel image sensors based on lead halide perovskite nanowires. *Adv. Mater.* **28**, 9713–9721 (2016).
24. Q. Zhang, M. M. Tavakoli, L. Gu, D. Zhang, L. Tang, Y. Gao, J. Guo, Y. Lin, S. F. Leung, S. Poddar, Y. Fu, Z. Fan, Efficient metal halide perovskite light-emitting diodes with significantly improved light extraction on nanophotonic substrates. *Nat. Commun.* **10**, 1–9 (2019).
25. Q. Zhang, D. Zhang, L. Gu, K. H. Tsui, S. Poddar, Y. Fu, L. Shu, Z. Fan, Three-dimensional perovskite nanophotonic wire array-based light-emitting diodes with significantly improved efficiency and stability. *ACS Nano* **14**, 1577–1585 (2020).
26. S. Il Kim, K. H. Lee, H. A. Mun, H. S. Kim, S. W. Hwang, J. W. Roh, D. J. Yang, W. H. Shin, X. S. Li, Y. H. Lee, G. J. Snyder, S. W. Kim, Dense dislocation arrays embedded in grain boundaries for high-performance bulk thermoelectrics. *Science* **348**, 109–114 (2015).
27. B. Qin, D. Wang, X. Liu, Y. Qin, J. F. Dong, J. Luo, J. W. Li, W. Liu, G. Tan, X. Tang, J. F. Li, J. He, L. D. Zhao, Power generation and thermoelectric cooling enabled by momentum and energy multiband alignments. *Science* **373**, 556–561 (2021).
28. Z. Wang, P. Fiorini, V. Leonov, C. Van Hoof, Characterization and optimization of polycrystalline Si 70% Ge 30% for surface micromachined thermopiles in human body applications. *J. Microelectromech. Syst.* **19**, 094011 (2009).
29. A. Roncaglia, M. Ferri, Thermoelectric materials in MEMS and NEMS: A review. *Sci. Adv. Mater.* **3**, 401–419 (2011).

Acknowledgments: We thank R. Ho, Y. Zhang, and A. H. K. Wong from Material and Characterization Preparation Facility (MCPF) at HKUST for technically assisting in acquiring SEM images. We also acknowledge the support from the Center for 1D/2D Quantum Materials and the State Key Laboratory of Advanced Displays and Optoelectronics Technologies at HKUST. **Funding:** This work was funded by the Science and Technology Plan of Shenzhen nos. JCYJ20170818114107730 and JCYJ20180306174923335; the Hong Kong Research Grant Council General Research Fund project nos. 16205321, 16214619, and 16206020; Innovation Technology Fund GHP/014/19SZ; Guangdong-Hong Kong-Macao Intelligent Micro-Nano Optoelectronic Technology Joint Laboratory project no. 2020B1212030010; Foshan Innovative and Entrepreneurial Research Team Program 2018IT100031; and Beijing Institute of Collaborative Innovation Exploratory Fund no. BICI22EG02. **Author contributions:** Conceptualization: Z.F. and Y.D. Methodology: Y.D., G.L., Z.L., Y.Z., and X.Q. Device fabrication: Y.D., G.L., Z.L., X.Q., B.R., and Z.W. Material optimization: G.L. and C.C. Supervision: Z.F. and B.H. Writing, review, and editing: Y.D., G.L., Z.L., Y.Z., Q.Z., B.H., and Z.F. **Competing interests:** The authors declare that they have no competing interests. **Data and materials availability:** All data needed to evaluate the conclusions in the paper are present in the paper and/or the Supplementary Materials.

Submitted 4 May 2022

Accepted 15 July 2022

Published 31 August 2022

10.1126/sciadv.abq8432

Uncooled self-powered hemispherical biomimetic pit organ for mid- to long-infrared imaging

Yucheng DingGongze LiuZhenghao LongYu ZhouXiao QiuBeitao RenQianpeng ZhangCheng ChiZhu'an WanBaoling HuangZhiyong Fan

Sci. Adv., 8 (35), eabq8432. • DOI: 10.1126/sciadv.abq8432

View the article online

<https://www.science.org/doi/10.1126/sciadv.abq8432>

Permissions

<https://www.science.org/help/reprints-and-permissions>

Use of this article is subject to the [Terms of service](#)